nature communications

Article

https://doi.org/10.1038/s41467-025-64377-z

Structural characterization of an extracellular contractile injection system from *Photorhabdus luminescens* in extended and contracted states

Received: 20 April 2025

Accepted: 16 September 2025

Leyre Marín-Arraiza[1], **Aritz Roa-Eguiara**[1], **Tillmann Pape**[1,2], **Nicholas Sofos**[1,2], **Ivo Alexander Hendriks**[1], **Michael Lund Nielsen**[1,3], **Eva Maria Steiner-Rebrova**[1,4] & **Nicholas M. I. Taylor**[1] ✉

Contractile injection systems (CISs) are phage tail-like nanosyringes that mediate bacterial interactions by puncturing target cell membranes. Within these systems, Photorhabdus Virulence Cassettes (PVCs) can translocate toxins across eukaryotic target cell membranes and have been engineered to deliver diverse protein cargoes into non-natively-targeted organisms. Despite the structural insights into several CISs, including one PVC from *P. asymbiotica*, information on PVCs from other species and details on the contraction mechanism remain limited. Here, we present the single-particle cryo-electron microscopy structure of *Pl*PVC1, a PVC from the nematode symbiont and insect pathogen *Photorhabdus luminescens DJC*, in both extended and contracted states. This particle displays distinct structural features that differ from other CISs, such as a cage surrounding the central spike, a larger sheath adaptor, and a plug exposed to the tube lumen. Moreover, we present the structures of the *Pl*PVC1 fiber and the baseplate of the contracted particle, yielding insight into the contraction mechanism. This study provides structural details of the extended and contracted states of the *Pl*PVC1 particle and supports the model in which contraction is triggered. Furthermore, it facilitates the comparison of *Pl*PVC1 with other CISs and expands the scope of engineering opportunities for future biomedical and biotechnological applications.

Microbial communities coexist and compete in their natural environments by interacting with their surroundings and other organisms[1]. These interactions often involve the translocation of macromolecules across cell membranes, mediating processes such as cellular communication and defense[2,3]. To facilitate this, many bacterial species have evolved a plethora of specialized machineries, the contractile injection systems (CISs), macromolecular nanosyringes distinct from one another but evolutionarily related to bacteriophage contractile tails[4]. These particles share a common structure consisting of a contractile sheath wrapped around a rigid tube, sharpened with a central spike, an

---

[1]Novo Nordisk Foundation Center for Protein Research, ICMM, Faculty of Health and Medical Sciences, University of Copenhagen, Copenhagen, Denmark. [2]Core Facility for Integrated Microscopy, Faculty of Health and Medical Sciences, University of Copenhagen, Copenhagen, Denmark. [3]Evosep Biosystems, Odense, Denmark. [4]Biomedical Centre, Department of Experimental Medical Science, Faculty of Medicine, University of Lund, Lund, Sweden.
✉e-mail: nicholas.taylor@cpr.ku.dk

assembly used for payload delivery[4]. The central spike is surrounded by a baseplate complex equipped with fibers for host recognition. The baseplate triggers contraction upon specific sensing of the target cell through the fiber network[5]. Contraction of the sheath drives the spiked tube outward, piercing the target cell membrane and injecting the payload.

Based on the anchoring mechanism of the baseplate to the membrane prior to action, bacterial CISs are commonly classified into type VI secretion systems (T6SSs) and extracellular contractile injection systems (eCISs). T6SSs are cell-wall-anchored CISs, widespread among Gram-negative bacteria[6], which deliver bacterial effectors into target prokaryotic or eukaryotic cells by being pushed out of the bacterial membrane[7,8]. In contrast, eCISs attack target cells from the extracellular environment. Several eCISs have been studied, each produced by different microorganisms and exhibiting distinct structural and functional features. Tail-like bacteriocins, or tailocins, are a broad family of eCISs[9], with the most well-studied example being the R-pyocin encoded by *Pseudomonas aeruginosa*[10,11]. R-pyocins bind to the receptor sites on the lipopolysaccharide of the target cell[12], and disrupt the membrane potential after puncturing of the cell membrane[13]. Metamorphosis-associated contractile structures (MACs), produced by *Pseudoalteromonas luteoviolacea*, arrange in ordered bundles[14] and carry effectors that are necessary to induce metamorphosis[15] and kill eukaryotic cells[16]. The well-characterized antifeeding prophage (AFP), produced by *Serratia entomophila*, acts as a delivery vehicle for the insecticidal toxin Afp18 and causes amber disease in the New Zealand grass grub[17–19]. Recently, a bacterial CIS found in *Algoriphagus machipongonensis* (AlgoCIS) was shown to exhibit structural differences compared to canonical contractile systems, presenting a cap adaptor, a plug harbored inside the tube lumen, and a cage-like structure around the spike[20].

Photorhabdus Virulence Cassettes (PVCs) are eCISs produced by bacteria of the *Photorhabdus* genus, which can translocate toxins across eukaryotic target membranes[21,22]. Different *Photorhabdus* species encode distinct copies of *pvc* operons in their genome, each associated with unique putative effector genes[23,24]. Notably, PVC-like genes are broadly distributed in the genomes of both prokaryotes and archaea[25,26], suggesting that these systems may represent an ancient mechanism contributing to microbial evolution and functional specialization[23]. The cryo-electron microscopy (cryo-EM) structure of PVCpnf, a PVC from *P. asymbiotica*, is morphologically similar to a contractile phage tail[27], and its target specificity is mediated by the recognition of cellular receptors by the tail fibers. These fibers can be genetically engineered to retarget the particle against non-natively-targeted organisms with high efficiency[28]. Moreover, PVCpnf is being studied for its potential to load diverse protein cargoes, which could be delivered to different targeted cells, both in vitro and in vivo[28,29]. This programmable capability provides the opportunity to customize PVCs for specific therapeutic applications.

Currently, structural and functional studies of PVCs are limited to PVCpnf from *P. asymbiotica*, and no cryo-EM structures have been reported for PVCs from other *Photorhabdus* species. Given that *P. luminescens* is a nematode symbiont and insect pathogen[30] that encodes six *pvc* operons in its genome[17,23,24], the characterization of PVCs from this species could significantly contribute to our understanding of the potential role of eCISs in symbiosis and infection.

In this study, we use cryo-EM to characterize the high-resolution structure of a PVC particle from *Photorhabdus luminescens DJC* (*Pl*PVC1), in both its extended and contracted states, providing critical insights into its architecture and function. *Pl*PVC1 has an associated putative effector showing sequence similarity to the known insecticidal toxin SepC[17], hinting at a possible in vivo role for this cluster. Furthermore, *Pl*PVC1 particles were easy to express and stable, facilitating their future use in possible downstream applications. This system resembles other phage tail-like particles, but with distinct structural features, such as the presence of a cage surrounding the central spike, a larger sheath adaptor, and a plug exposed to the tube lumen. Furthermore, the structures of the fiber and the baseplate of the contracted *Pl*PVC1 particle were solved, providing a comprehensive framework for understanding the contraction mechanism. The detailed structural characterization and comparison of the extended and contracted states support the model in which contraction is triggered upon target cell recognition by the fibers. These findings significantly advance our understanding of PVCs and contribute to their promising customization as biomedical tools, from biocontrol to precision therapy.

Results

Overall structure of the *Pl*PVC1 particle

The *pvc* operon 1 from *Photorhabdus luminescens DJC* was cloned for expression in *Escherichia coli*. It comprises 16 open reading frames encoding the proteins that constitute the *Pl*PVC1 particle (Pvc1 to Pvc16) (Fig. 1a, Supplementary Fig. 1, Supplementary Table 1). Mass spectrometry (MS) confirmed the presence of all proteins in the purified sample. After expression, fully assembled *Pl*PVC1 particles were visualized with negative-staining transmission electron microscopy (NS-TEM) (Supplementary Fig. 2a). The length of purified *Pl*PVC1 particles in the extended state was heterogeneous, with an average particle length of ~280 nm (Supplementary Fig. 2b, Supplementary Table 2). Single-particle cryo-EM was used to determine the high-resolution structures of the *Pl*PVC1 particle components (Supplementary Figs. 3 and 4, Supplementary Table 3). *Pl*PVC1 shares a similar architecture with other phage tail-like particles[11,19,20,27]: a baseplate surrounded by tail fibers network and equipped with a central spike sharpened at the tip, a contractile trunk composed of sheath and inner tube, and a terminal cap at the apical end (Fig. 1b, c, Supplementary Fig. 2a). The *Pl*PVC1 particle generally follows 6-fold symmetry along its structure, with symmetry mismatches between the baseplate (6-fold), central spike (3-fold), and spike tip (1-fold). In the extended state, the outer diameter of the sheath reaches 162 Å, enclosing the inner tube, which has an outer and inner diameter of 80 Å and 45 Å, respectively. At the baseplate level, the particle diameter expands up to 280 Å (Fig. 1b). Symmetry-based single-particle reconstruction was divided into regions – cap, baseplate, central spike, and fiber – and mask-based processing was used to improve the density resolution of specific parts (Supplementary Figs. 3 and 4, Supplementary Table 3).

The cap and baseplate density maps in the extended state were reconstructed to overall resolutions of 2.5 Å and 2.7 Å, respectively, applying 6-fold symmetry. The central spike was reconstructed to 2.8 Å by applying 3-fold symmetry. Using these cryo-EM maps, 14 proteins could be located in the *Pl*PVC1 particle. For 12 of these proteins, partial or full atomic models could be built (Fig. 1a, b, Supplementary Fig. 5a). Proteins Pvc14 and Pvc15, which were present in the sample as verified by MS, could not be located in any density map and thus were not modeled. The fibers were reconstructed individually, by local refinement in a symmetry-expanded particle set, to a resolution ranging from 4 Å to 6 Å. The AlphaFold model of a trimer of the fiber protein Pvc13 was fitted into the fiber density map, and the interaction between baseplate and fiber was built and refined (Supplementary Figs. 3, 4, 6a, Supplementary Table 3).

Contraction of the *Pl*PVC1 particle was induced by exposing purified particles to 3 M urea[31,32] (Fig. 1d, Supplementary Fig. 2c). The contracted sheath was solved at 3.1 Å, and atomic models of the contracted sheath proteins were built (Supplementary Fig. 5b). The baseplate of the contracted particle was solved at a resolution ranging from 4 Å to 10 Å, and atomic models of the baseplate proteins were rigid-body fitted in the density map (Supplementary Figs. 3 and 4, Supplementary Table 3).

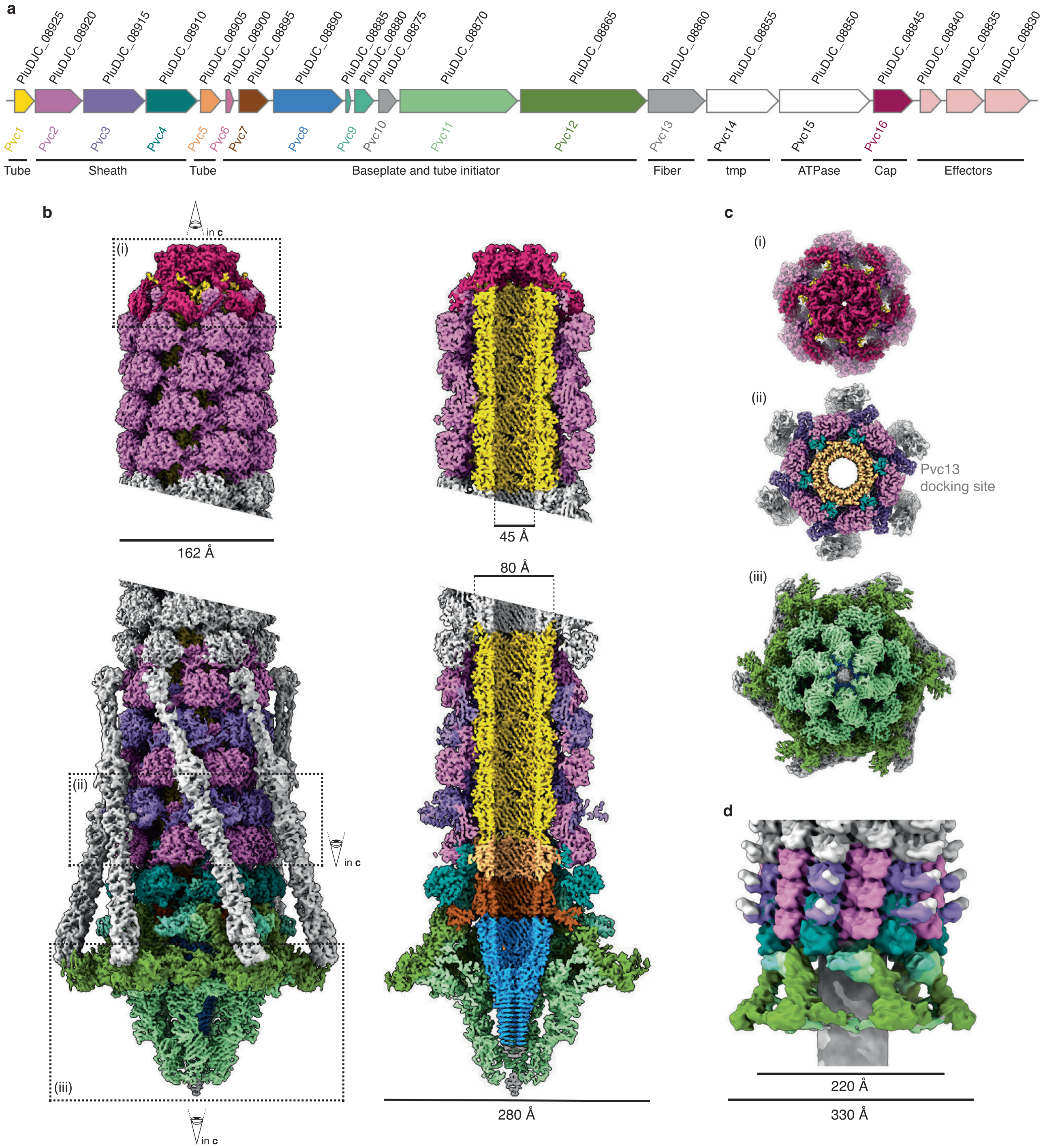

Fig. 1 | Overall cryo-EM structure of the *Pl*PVC1 particle in its extended and contracted states. a Schematic representation of the genomic organization of the *Plpvc1* cluster. The gene accession numbers are shown above the corresponding genes. **b** Cryo-EM map of the *Pl*PVC1 particle in its extended state (*left*) and a sliced view (*right*). The different structural subunits are colored according to the color code in (**a**). **c** Horizontal cut-out views of the marked sections i-iii in (**b**); (i) Top view of the terminal cap; (ii) bottom view of the fiber docking site; (iii) bottom view of the baseplate. **d** Cryo-EM map of the *Pl*PVC1 particle in its contracted state, filtered to 10 Å. The different structural subunits are colored according to the color code in (**a**).

*Pl*PVC1 baseplate

The overall architecture of the *Pl*PVC1 baseplate in its extended state is similar to the one in PVCpnf[27] and AFP[19] particles and resembles a streamlined T4 inner baseplate[5] (Fig. 2a, Supplementary Fig. 7). The *Pl*PVC1 baseplate complex exhibits a 6-fold symmetrical assembly of the wedges (Pvc11 and Pvc12) surrounding the trimeric central spike (Pvc8), sharpened with the spike tip (Pvc10). The central spike is attached to the inner tube and is surrounded by the baseplate wedges, which transition into the sheath-tube trunk through the sheath adaptor (Pvc9) (Fig. 2a).

Pvc11 and Pvc12 arrange in heterodimers, similarly to the phage T4 $[gp6]_2$-gp7 helical core bundle[5]. This $[gp6]_2$-gp7-like core bundle in the baseplate wedges is conserved among other eCIS[11,19,20,27], highlighting its importance in baseplate assembly and functionality. In the case of

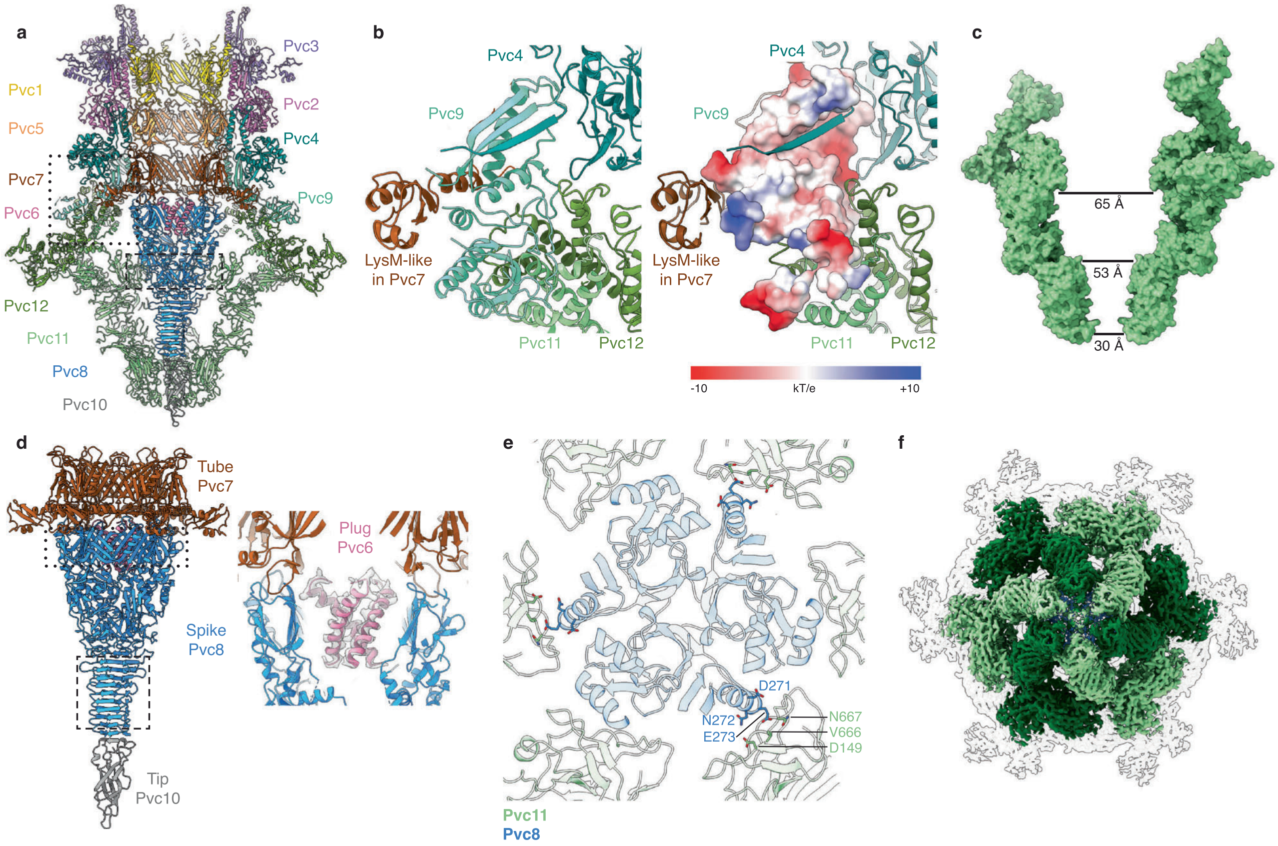

Fig. 2 | Organization and atomic model of the *Pl*PVC1 baseplate in its extended state. **a** Side cut-out view of the atomic model of the baseplate complex in the *Pl*PVC1 particle. The first layers of the sheath and tube are also shown. **b** Zoom-in of the marked section in the dotted-line rectangle in (**a**), showing interactions between the sheath adaptor Pvc9 and the sheath initiator Pvc4, the LysM-like domain in Pvc7, and the baseplate wedge proteins Pvc11 and Pvc12; together with the same representation but with the electrostatic surface of the Pvc9 monomer contoured at potential ±10 kT/e. **c** Side cut-out view of the surface representation of the spike cage in the *Pl*PVC1 baseplate. Distances between opposite Pvc11 subunits are indicated. **d** Side view of the atomic model of the tube initiator, the central spike, and the spike tip in the *Pl*PVC1 particle. The dotted-line rectangle marks the β-barrel conformation, transitioning between C6 and C3 symmetry. The dashed-line rectangle marks the cone-shaped β-helix of the spike. Zoom-in of the plug protein Pvc6 in the lumen of the inner tube, showing the cryo-EM density and the ribbon diagram of the built atomic model. **e** Top cut-out view of the marked section in the dashed-line rectangle in (**a**), showing the main interactions between Pvc11 and the central spike Pvc8 in the upper part of the spike. Residues involved in the main interactions are labeled and shown as sticks. **f** Bottom view of the configuration of the cage around the central spike, with Pvc11 monomers colored according to their interaction with Pvc8; light green: contacting, dark green: non-contacting.

*Pl*PVC1, Pvc12 resembles a combination of T4 gp6 in the "gp6B" position and gp7, whereas Pvc11 is similar to T4 gp6 in the "gp6A" position (Supplementary Fig. 8a).

The sheath adaptor Pvc9 in *Pl*PVC1 is homologous to Pvc9 in PVCpnf, Afp9, Alg9, and gp25 in phage T4 (Supplementary Fig. 8b). Interestingly, Pvc9 is longer in the *Pl*PVC1 particle than in those other CISs and protrudes on top of Pvc12 and Pvc11 (Fig. 2b, Supplementary Fig. 9, Supplementary Tables 4 and 5). As seen in other CISs[5,19,20,27], the sheath adaptor acts as an interface between the baseplate wedges and the trunk of the particle, facilitating sheath orientation and assembly via several interactions between Pvc9 and baseplate, sheath, and tube proteins. Pvc9 extensively interacts with the sheath initiator Pvc4, the tube initiator Pvc7, and the baseplate wedge proteins Pvc11 and Pvc12, via predominantly charged and polar residues (Fig. 2b). Interaction-prediction analysis[33,34] predicted Pvc9 interplay with proteins in the region where the sheath adaptor interacts with Pvc4, Pvc7, Pvc11, and Pvc12. Additionally, isolated interactions with carbohydrates were predicted[33,34] for some residues in the protruded region, which is exposed toward the outer part of the particle (Supplementary Fig. 8c).

*Pl*PVC1 baseplate cage

The baseplate of *Pl*PVC1 features an expanded cage around the central spike, formed by extensions of the protein Pvc11 (Fig. 2a, c). The cavity of the cage ranges between 65 Å and 30 Å in diameter (Fig. 2c). This cage-like structure was not determined in PVCpnf[27] or in AFP[19] but was identified in the AlgoCIS particle[20] (Supplementary Figs. 7, 8d, 9, Supplementary Tables 4 and 5). When compared to Alg11, both Pvc11 and Alg11 present an analogous fold in their N-terminal and C-terminal regions, conserved area of interaction with Pvc12 or Alg12, respectively (Supplementary Figs. 8d and 10). The folding of the cage extensions is also similar in both cases, although it is shorter in Pvc11 (Supplementary Fig. 8d). The inner surface of the Pvc11 cage is mainly negatively charged, in contrast to the surrounded spike, which presents a positively charged outer surface (Supplementary Fig. 8e). Structure-based bioinformatic analysis[35,36] identified structural homology between carbohydrate-binding proteins and Pvc11 extensions, consistent with analogous observations reported for Alg11[20]. In addition, interaction-prediction analysis[33,34] suggested potential lipid and carbohydrate interaction interfaces within the cage extensions (Supplementary Fig. 8f).

*Pl*PVC1 central spike

The central spike of *Pl*PVC1 is composed of three copies of the protein Pvc8. It extends from the inner tube and is sharpened at the tip by a single copy of the spike tip protein Pvc10 (Fig. 2a, d). Three main interaction interfaces are observed between Pvc8 and Pvc11, primarily involving polar (N667 in Pvc11; N272 in Pvc8) and charged (D149 in Pvc11; D271 and E273 in Pvc8) residues (Fig. 2e). These interfaces facilitate the association between the central hub and the baseplate wedges, leading to the specific arrangement of Pvc11 around Pvc8 in an alternating pattern of contacting and non-contacting monomers. This arrangement is a consequence of the symmetry mismatch between the spike (3-fold) and the baseplate wedges (6-fold) and is likely important for baseplate assembly and stabilization (Fig. 2f).

Similar to VgrG in T6SS[6], the central spike protein Pvc8 contains regions homologous to central hub proteins from phage T4. The N-terminal region of Pvc8, which functions as the symmetry adaptor[5,37], correlates with gp27, while the C-terminal region is homologous to gp5 (Supplementary Fig. 8g). The upper part of the central spike adopts a β-barrel conformation, featuring the folding seen in the tube proteins, allowing the transition between the 6-fold symmetry of the tube initiator hexamer and the 3-fold symmetry of the spike trimer. The lower part of the central spike folds in a cone-shaped manner, creating a rigid structure stabilized by several integrated β-strands, and binds to the spike tip protein Pvc10, a homolog of gp5.4 in phage T4 (Fig. 2d). We attempted to desymmetrize the spike tip density, but this was not possible, and no atomic model was built for Pvc10. Thus, the AlphaFold prediction of Pvc10 was docked into the tip density, following the β-strand folding of Pvc8 and using the structure of T4 gp5 and T4 gp5.4 in their C-terminal regions as a reference (Supplementary Fig. 6b). Some phages have been reported to puncture cell membranes with ion-loaded spikes[37,38]. To determine possible loading of ions in the spike tip of *Pl*PVC1, the sequence and predicted structure of Pvc10 were analyzed and compared to the sequence and structure of gp5.4. No conserved residues with potential involvement in iron coordination were found in Pvc10, in contrast to gp5.4, where an iron atom is coordinated by several histidine residues [PDB: 4KU0]. However, two conserved residues in Pvc10, S34 and D49, correlate with two conserved residues in gp5.4, T25 and D41, which are believed to be involved in sodium binding (Supplementary Fig. 8h).

*Pl*PVC1 plug

A helical density was identified within the cavity of the central spike, exposed toward the lumen of the inner tube (Fig. 2d). Local refinement applying 3-fold symmetry allowed the structural identification of three copies of the plug protein Pvc6. Homologs of this protein could also be identified in corresponding regions of other particles[19,20,27] (Supplementary Fig. 9, Supplementary Tables 4 and 5). A partial atomic model of Pvc6 could be constructed, from residues 24 to 51, a region that adopts an α-helical structure. Pvc6 features a trimeric hydrophobic inner core and a hydrophilic surface, which allows interaction with Pvc8 in its gp27-like region (Supplementary Fig. 8i, j). Previous structural and functional studies on plug homologs, such as Pvc6 in PVCpnf, Afp6 in AFP, and Alg6 in the AlgoCIS particle, indicated that they are crucial for particle assembly and functionality[19,20,27]. To further validate this, a *Pl*PVC1ΔPvc6 mutant was generated and analyzed. No assembled particles could be purified (Supplementary Fig. 8k).

*Pl*PVC1 trunk: inner tube

The tube of the *Pl*PVC1 particle is composed of three different tube proteins (Pvc7, Pvc5, Pvc1), which assemble a structure with inner and outer diameters of 45 Å and 80 Å, respectively (Fig. 1b). The first layer of the tube, that contacts the central spike Pvc8, is formed by the tube initiator Pvc7, followed by a ring of Pvc5, and then continued by consecutive stacked layers of Pvc1 until the apical end (Figs. 1b and 3a).

Pvc7, Pvc5, and Pvc1 proteins share a common fold, similar to their corresponding homologs gp48, gp54, and gp19 in phage T4 (Supplementary Fig. 11a, b). Additionally, Pvc7 features a LysM-like domain[39], as gp53 in phage T4 and the glue protein in pyocin R2. This domain is also present in the tube initiators of AFP, PVCpnf, and AlgoCIS (Supplementary Fig. 11c). The LysM-like domain extends in the C-terminal region of Pvc7 and interacts extensively, in a mainly negatively charged interface, with the baseplate wedge protein Pvc12 and the sheath protein Pvc4, playing an important role in the stabilization of the baseplate-trunk interface (Fig. 3b, Supplementary Fig. 11d).

The stacking of tube proteins relies on conserved β-loop intercalations between them (Supplementary Figs. 10 and 11e). Each Pvc1 subunit interacts with two subunits in the layer above and two in the layer below (Fig. 3c). Following the same pattern, Pvc5 and Pvc7 subunits interact with Pvc1-Pvc7 and with Pvc5-Pvc8, respectively. This β-barrel-like arrangement lengthens the whole tube from central spike to cap, providing a compact and rigid structure. Notably, the inner surface of the tube lumen is negatively charged (Supplementary Fig. 11f), which in eCISs is believed to be involved in the efficient packing and release of cargoes loaded inside the trunk[19,27,40].

*Pl*PVC1 trunk: sheath

The sheath of the *Pl*PVC1 particle is formed by three different proteins (Pvc4, Pvc2, Pvc3), which surround the inner tube, expanding the outer diameter of the trunk to 162 Å (Figs. 1b and 3a). Pvc2, Pvc3, and Pvc4 share a common fold, similar to gp18 in phage T4 and sheath proteins in other eCIS (Supplementary Fig. 12a, b). When compared to the other sheath proteins, Pvc3 presents an extra knob, formed by residues 64–117 and 225–278, which is believed to act as a fiber docking domain for the retracted fibers in the extended state of the particle (Fig. 1c, Supplementary Fig. 12a).

The sheath is initiated by the sheath initiator Pvc4, which interacts with the sheath adaptor Pvc9, the LysM-like domain in Pvc7, Pvc5 in the first layer of the tube, and Pvc2 in the first layer of the sheath. These interactions occur at electrostatically charged surfaces on the contacting interfaces, and the involved residues from Pvc4 are mostly conserved (Supplementary Figs. 10 and 12c, d). In the following levels, the sheath comprises alternate layers of Pvc2 and Pvc3, finishing with stacked layers of Pvc2 in the apical end, all assembled with a helical rise of 39.8 Å and a twist of 20.1° (Figs. 1b and 3a). The alternating Pvc2-Pvc3 pattern seems to be influenced by the assembly of the retracted fibers (Fig. 1b, c), as Pvc3 is the only sheath protein with a presumed fiber docking domain (Supplementary Fig. 12a). The exact layer at which Pvc3 terminates could not be determined due to length heterogeneity in a mixed population of particles.

The sheath assembly relies on conserved β-strand intercalations, or handshakes, between sheath proteins. The first intercalation happens between the sheath adaptor Pvc9 and the sheath initiator Pvc4, which allows for the docking of the sheath and baseplate together (Fig. 3d, Supplementary Fig. 12c). Analogously, Pvc4 interacts with Pvc2, which sequentially interacts with Pvc3. These consecutive handshakes propagate in each sheath layer, from baseplate to cap, stabilizing the sheath assembly in the *Pl*PVC1 particle (Fig. 3d).

The sheath and tube proteins interact along the particle. Pvc2, Pvc3, and Pvc4 feature an attachment helix through which interactions with the tube proteins Pvc1 and Pvc5 occur (Fig. 3e). The tube-sheath interplay seems to be driven by the specific distribution of charged and polar residues at the contacting interfaces, contributing to the stabilization of the particle in its extended state, a structural feature that is conserved across eCISs[19,27,40].

*Pl*PVC1 terminal cap

The extended *Pl*PVC1 particle terminates with the cap complex at the apical end. This complex is composed of six monomers of the protein Pvc16 (Figs. 1c and 4a). Each Pvc16 monomer consists of two main domains, the N-terminal domain (NTD) and the C-terminal domain (CTD), connected by a middle loop with a β-strand (Fig. 4b). The NTD of Pvc16 has a similar fold to gp15 from phage T4[41] but contains an extra conserved α-helix that allows the closure of the inner tube down to a diameter of 6.7 Å, as has also been observed for Pvc16 of PVCpnf[27] and Afp16[19] (Fig. 4c, Supplementary Fig. 13a–c). There are multiple

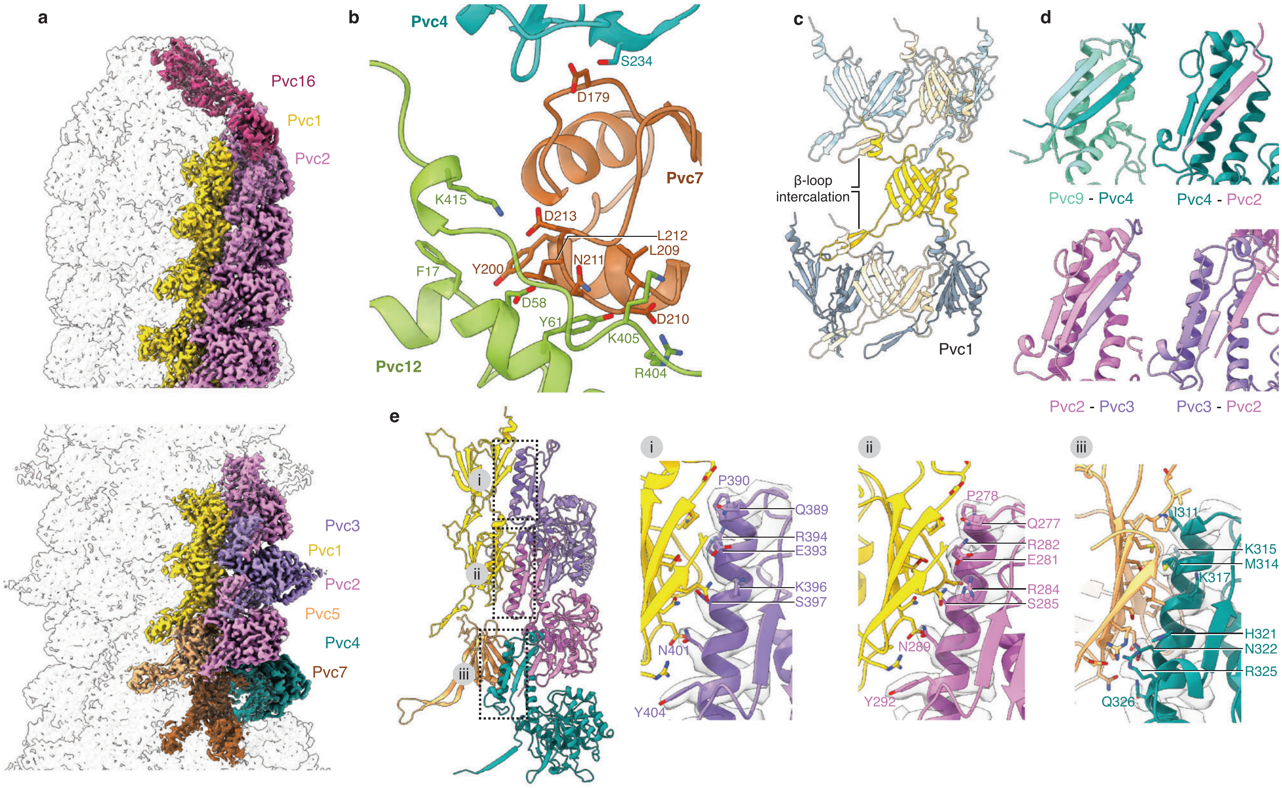

Fig. 3 | Organization and atomic model of the *Pl*PVC1 tube and sheath in its extended state. a Cryo-EM map of the extended *Pl*PVC1 particle with the tube and sheath subunits colored, visualized at the level of the cap (*top*) and the baseplate (*bottom*). **b** Zoom-in of the main interactions of the LysM-like domain in Pvc7 with the sheath initiator Pvc4 and the baseplate wedge protein Pvc12. Residues involved in the main interactions are labeled and shown as sticks. **c** β-loop intercalations within Pvc1 subunits in different stacked layers of the tube. One central Pvc1 subunit is represented in yellow, interacting with two Pvc1 subunits in the layer above (light blue) and two in the layer below (gray). **d** Zoom-in of the β-intercalation handshakes between sheath layers. The β-strand exchange occurs along all layers, from baseplate to cap. **e** Visualization of conserved interactions between tube and sheath subunits, showing the cryo-EM density and the atomic models represented as ribbon diagrams. Selected residues in the attachment helices of the different sheath subunits are labeled and shown as sticks. (i) Pvc3–Pvc1, (ii) Pvc2–Pvc1, and (iii) Pvc4–Pvc5.

interactions between the Pvc16 subunits and the tube and sheath proteins. The NTD of each Pvc16 monomer interacts with two different subjacent Pvc1 neighboring subunits in their N-terminal region, leading to a distinct conformation of Pvc1 in the apical layer (Fig. 4d, Supplementary Fig. 13d, e). The middle loop of each Pvc16 monomer interacts via β-strand intercalation with the C-terminal region of the immediately below Pvc2 subunit in the top layer of the sheath, while the CTD of the Pvc16 monomer makes a turn and interacts with the N-terminal region of the adjacent Pvc2 subunit (Fig. 4e, Supplementary Fig. 13d, e). These conserved interactions allow for the docking of Pvc16 into the upmost sheath layer in a handshake manner, closing and stabilizing the particle in its extended state.

*Pl*PVC1 contracted sheath and baseplate of the contracted particle

In order to investigate the conformational changes that occur when particles get activated and sheath contraction is initiated, the contraction process was mimicked in vitro by exposing purified particles to 3 M urea[31,32] (Fig. 1d, Supplementary Fig. 2c). As in other CISs[5,11,19,27,40], the sheath undergoes conformational changes upon contraction, without losing the handshakes between subunits, which seemingly maintains the integrity of the sheath (Fig. 5a, b; Supplementary Figs. 5b, 14a). Contraction leads to vertical compression of the sheath, with a helical rise of 17.5 Å and a twist of 31.7°, and to an expansion in both the outer and inner diameters, from 162 Å to 220 Å in the former, and from 80 Å to 110 Å in the latter (Fig. 5b, Supplementary Fig. 14b). This is driven by conformational transitions in the sheath proteins, which rearrange their C- and N-termini by rigid-body rotation, compared to their conformation in extended state (Supplementary Fig. 14c). These rearrangements allow sheath monomers to slide over one another, opening the diameter of the sheath and enabling tube-sheath detachment and tube ejection for target cell membrane perforation.

The density map of the baseplate of the contracted *Pl*PVC1 particle could be solved at a resolution ranging from 4 Å to 10 Å, depending on proximity to the sheath or to wedges periphery (Supplementary Figs. 3 and 4, Supplementary Table 3). Although a complete de novo atomic model could not be built for the baseplate of the contracted particle, rigid-body fitting of the sheath adaptor Pvc9 and baseplate wedge proteins Pvc11 and Pvc12 into the density allowed for the building of a partial atomic model (Fig. 5c). This fitted model suggested that, upon contraction, the baseplate wedge proteins Pvc11 and Pvc12 undergo lateral dissociation and diameter expansion, coupled with a pivoting motion toward the periphery of the particle (Fig. 5d), similar to rearrangements reported in the AFP particle[19] and pyocin R2[11]. Notably, the sheath adaptor Pvc9 appeared to rearrange at the interface between the expanded baseplate and the sheath initiator Pvc4 (Fig. 5d), suggesting its role in transmitting the contraction signal from the baseplate to the sheath, launching the subsequent conformational changes in the sheath proteins, as observed for Afp9 in AFP[19] and gp25 in phage T4[5].

*Pl*PVC1 fiber

*Pl*PVC1 presents a set of six tail fibers, arranged in a retracted manner around the extended particle (Fig. 1b). Each fiber is composed of three intertwined copies of the Pvc13 protein and exhibits an arched topology, in which the C-terminus is folded toward the middle of the fiber

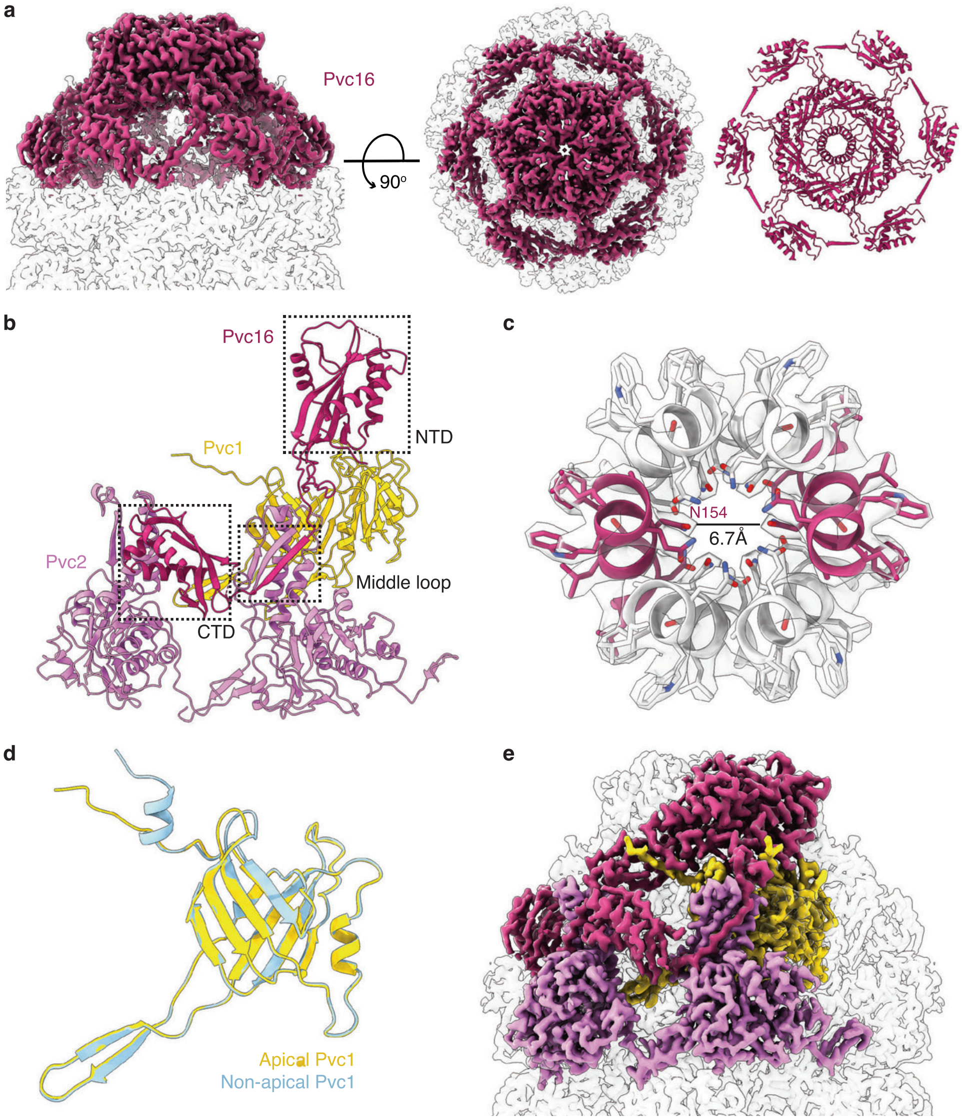

Fig. 4 | Organization and atomic model of the *Pl*PVC1 cap in its extended state. **a** Side and top views (*left and middle*) of the cryo-EM map of the *Pl*PVC1 terminal cap. The map region of the Pvc16 subunits is colored. Top view of the atomic model of the Pvc16 complex in ribbon diagram (*right*). **b** Zoom-in of a Pvc16 monomer interacting with Pvc1 and Pvc2 in the upmost layer of the particle in its extended state. The N-terminal domain (NTD), middle β-strand loop (middle loop), and C-terminal domain (CTD) of the Pvc16 monomer are marked with dashed-line rectangles. **c** Central ring of the terminal cap complex, showing the cryo-EM density and the ribbon diagrams, with fitted α-helices (residues 149–159 shown as sticks). Two opposite α-helices are colored in dark magenta as a reference. The aperture of the apical part of the *Pl*PVC1 particle is 6.7 Å, as measured by the distance between the amino acid N154 of opposing Pvc16 monomers. **d** Conformational comparison between the apical Pvc1 tube subunit in the top layer of the tube (yellow) and the non-apical Pvc1 tube subunit in the rest of the layers (blue). **e** Side view of the cryo-EM map of the *Pl*PVC1 terminal cap, showing the conserved β-intercalation handshake between Pvc16 and Pvc2 sheath subunits, together with the interaction between Pvc16 and the apical Pvc1 tube subunit.

(Fig. 6a, Supplementary Fig. 15a). Pvc13 sequence analysis showed an organization of the fiber into three main parts: the N-terminal region containing helical motifs with homology to fibers in other CISs[42], the central region with repetitive motifs homologous to adenoviruses fibers, and the C-terminal region with homology to host-binding domains of short tail fibers from bacteriophages (Supplementary Fig. 15b).

The AlphaFold model of the fiber, a trimer of Pvc13, was fitted into the density determined for the fiber in retracted conformation. The resolution was sufficient for recognizing domain segments of the fiber and for confident fitting of the AlphaFold model into the density (Fig. 6b; Supplementary Figs. 6a and 15a). Local refinement over the area of interaction between baseplate and fiber allowed for atomic modeling of this region (residues 29–55 in Pvc13 and residues 622–641, 686–708, 882–956 in Pvc12) (Fig. 6c). The interaction between baseplate and fiber happens between the C-terminal region of Pvc12, in the periphery of the baseplate wedge, and the N-terminal region of the Pvc13 trimer, region which folds into two conserved α-helices (Fig. 6c, Supplementary Fig. 15c). This interaction results in a predominantly hydrophobic and electrostatically neutral core in between the baseplate wedge and the fiber (Supplementary Fig. 15d), which might contribute to the orientation of the fiber in a retracted conformation in the extended state of the particle.

Discussion

Bacteria have evolved specialized contractile injection systems to invade and modulate target cells, all evolutionary related to bacteriophage contractile tails[4]. To date, several CISs have been broadly studied, and their high-resolution structures have been described[5,7,8,11,19,20,27,40,42]. The work here presents the single-particle

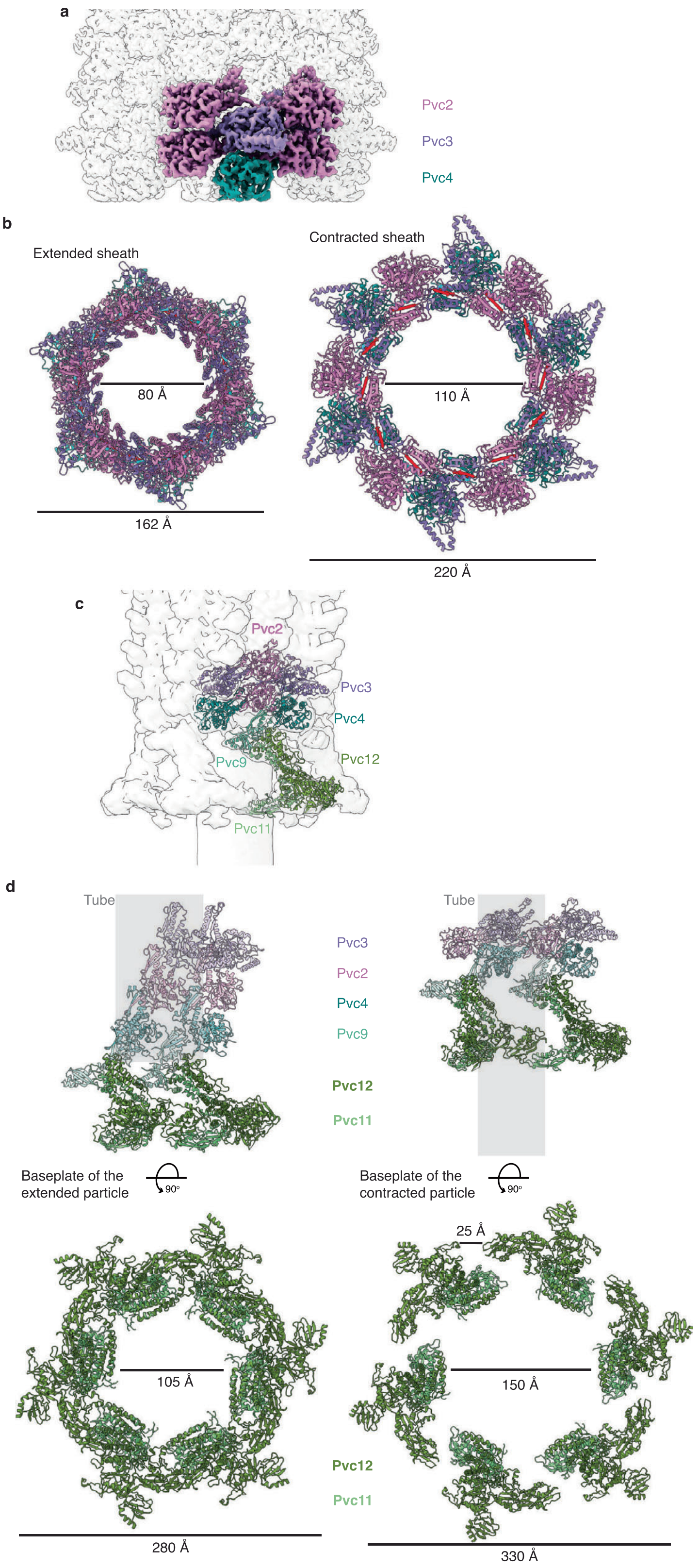

cryo-EM structure of a PVC particle from *Photorhabdus luminescens DJC* (*Pl*PVC1), in both its extended and contracted states, highlighting its structural relationship with other CISs, and provides a molecular framework for understanding its mechanism of action.

The *Pl*PVC1 particle has a contractile trunk with conserved handshakes and β-loop intercalations between the stacked sheath and tube subunits, and is stabilized at the apical end by the terminator cap complex. The wedges, Pvc11 and Pvc12, of the hexagonal baseplate in *Pl*PVC1 are assembled in a 6:6 stoichiometry around the trimeric central spike, Pvc8, which is sharpened by the monomeric spike tip, Pvc10. Interestingly, the *Pl*PVC1 particle features a longer sheath adaptor, Pvc9, which protrudes on top of the baseplate wedge proteins. This could lead to hypotheses of other roles for Pvc9, apart from organizing sheath orientation and assembly. Although analysis of the extra

Fig. 5 | Organization and atomic model of the *Pl*PVC1 sheath and baseplate in its contracted state. a Cryo-EM map of the *Pl*PVC1 sheath in contracted state, with sheath subunits colored. **b** Top view of the extended and contracted states of the sheath, with sheath subunits Pvc2, Pvc3, and Pvc4 represented as ribbon diagrams and diameter measurements. The β-strands involved in subunit intercalation are colored in red (β-strands in the C-terminal region) and cyan (β-strands in the N-terminal region). **c** Cryo-EM map of the *Pl*PVC1 baseplate in the contracted state of the particle, filtered to 10 Å, with fitted Pvc2, Pvc3, Pvc4, Pvc9, Pvc11, and Pvc12 subunits. Map-model Correlation Coefficient = 0.65. **d** Side view of the ribbon diagrams of two adjacent baseplate wedges (proteins Pvc11 and Pvc12), together with the first layers of the sheath (proteins Pvc9, Pvc4, Pvc2, and Pvc3), in extended and contracted states. The sheath proteins are represented in transparent colors. The baseplate wedge proteins are represented in solid colors. The tube is represented in light gray. Top view of the ribbon diagrams of baseplate wedges (proteins Pvc11 and Pvc12) in extended and contracted states, with measurements for diameter and separation of the wedges.

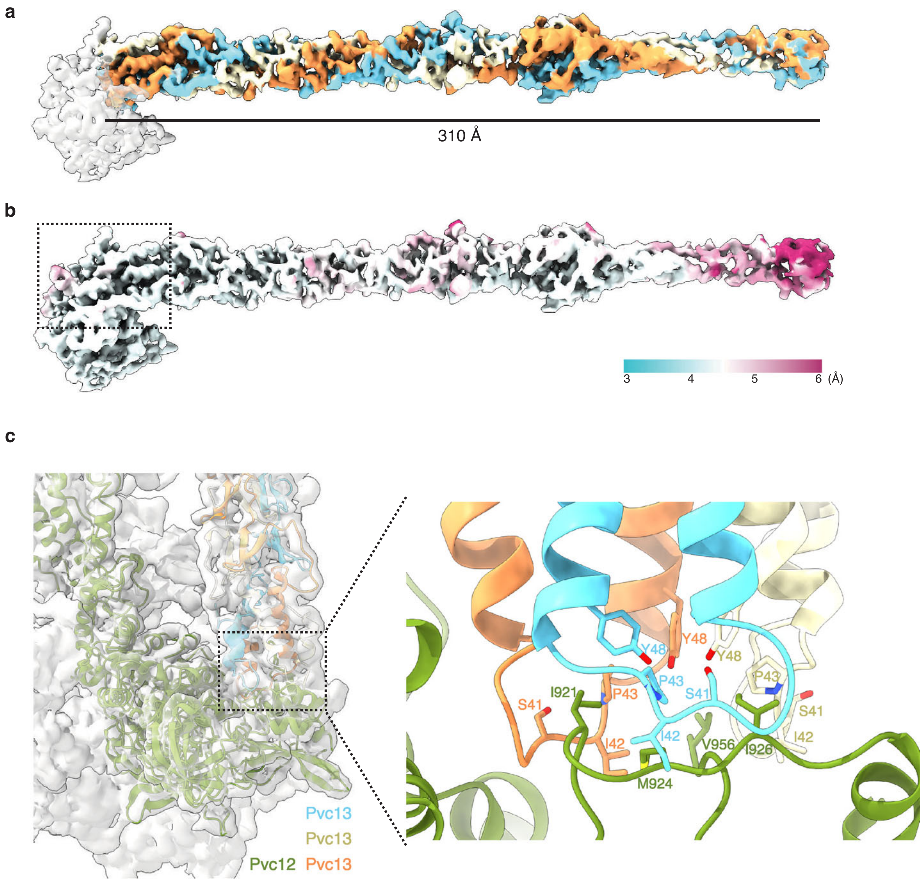

Fig. 6 | Structure of the *Pl*PVC1 fiber. a Cryo-EM map of the *Pl*PVC1 fiber showing the intertwined copies in the Pvc13 trimer. Each Pvc13 monomer is colored in cyan, yellow, and orange, respectively. **b** Cryo-EM map of the *Pl*PVC1 fiber colored by local resolution. The dashed-line rectangle marks the region where local refinement was applied to refine the interaction between the baseplate and the fiber. **c** Cryo-EM map and atomic model of the interaction between baseplate and fiber in *Pl*PVC1, with a close-up view of the dashed region in the figure. Pvc12 is colored in dark green. Each Pvc13 monomer is colored in cyan, yellow, and orange, respectively. Residues involved in the baseplate-fiber interaction are labeled and shown as sticks.

domain in the sheath adaptor Pvc9 was performed, the functionality of this protrusion remains ambiguous and requires further investigation. Two other remarkable features of the *Pl*PVC1 particle are the presence of a plug protein, Pvc6, in the cavity of the central spike exposed toward the lumen of the inner tube, and the existence of baseplate extensions in Pvc11 forming a cage around the central spike. The functionality of the cage remains unknown; however, our structure-based bioinformatic analyses are consistent with Xu et al.'s[20] results and their suggestion that the cage may contribute to particle-cell attachment. This hypothetical role for the cage-like structure warrants further experimental validation. In addition, our results also reinforce the importance of the plug protein in particle assembly, as no assembled particles were observed in the *Pl*PVC1ΔPvc6 mutant sample.

The structure of a PVC fiber has not been previously described at high resolution. In this study, the density map of the *Pl*PVC1 fiber in retracted conformation is solved at a resolution range of 4 Å to 6 Å, the AlphaFold model of the fiber is confidently fitted into the density, and the atomic interactions between baseplate and fiber are modeled. The limited resolution of the fiber density map may reflect the intrinsic flexibility of the fiber, which is consistent with the proposed role of the fibers in sensing and interacting with the target cell surface[4,27,28], functionality that likely requires a degree of mobility and conformational adaptability. Future studies addressing fiber dynamics and interactions with host receptors will be essential to fully understand their role in target recognition and activation of the contraction mechanism. Sequence analysis of the *Pl*PVC1 fiber showed divergence from phage tail fibers in the presence of homologous regions with fibers from eukaryotic viruses (adenoviruses), which suggests that the fiber protein Pvc13 could be a fusion protein derived from phage tail fibers and adenovirus fibers and reinforces the hypothesis of PVC particles, and related eCISs such as AFP and MACs, targeting eukaryotic organisms[16,19,27,28].

Extended and contracted structures of other eCISs have been reported, providing insight into the mechanism of contraction[11,19,20,27,40]. However, high-resolution structures of the baseplates in the contracted

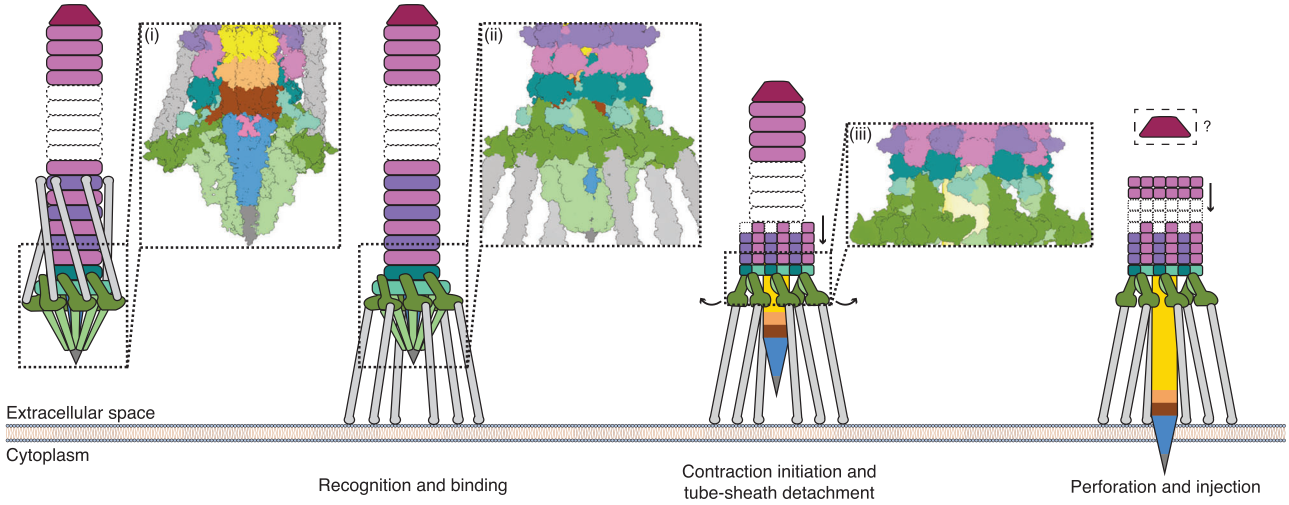

Fig. 7 | Schematic model for *Pl*PVC1 target recognition and contraction. Schematic representation of the proposed mechanism for *Pl*PVC1 contraction. The particle recognizes and binds specific receptors on the target cell membrane via its tail fibers. Rearrangements in the fibers lead to conformational changes in the baseplate, which sequentially trigger sheath contraction. Contraction of the sheath results in tube-sheath detachment, ejection of the inner tube, and perforation of the target cell membrane. (i) and (ii) are zoom-ins of the lower part of the particle in its extended state, (i) in a cut-out side view and (ii) in a full side view, where the plug protein Pvc6, the protrusions of the sheath adaptor Pvc9, and the cage-like structure formed by the baseplate wedge protein Pvc11 can be observed. (iii) Zoom-in of the baseplate wedges and the first layers of the sheath in the contracted state of the particle.

state remain incomplete in most cases. Here, we present a cryo-EM structure of the baseplate of the contracted *Pl*PVC1 particle, facilitating our understanding of the contraction mechanism in this particle and allowing the comparison with other eCISs. In vitro contraction of the *Pl*PVC1 particle established the molecular framework for studying protein rearrangements in the contracted state and for comparing it with the metastable extended state.

In a similar fashion to phage T4[5,32,43–45] and the AFP particle[19], the contraction signal is believed to be sensed at the level of the fibers, after recognition of specific receptors on the target cell membrane[28,46]. Subsequent changes in the orientation of the fibers are transmitted to the baseplate through Pvc12, leading to expansion of the baseplate wedges and pivoting toward the periphery of the particle. This mirrors the mechanism described by Desfosses et al. for AFP, where the baseplate wedges similarly swing outward upon activation[19]. Then, the contraction wave propagates toward the sheath until reaching the terminal part of the particle. This is coordinated by the sheath adaptor Pvc9, which structurally resembles Afp9[19] and plays a crucial role in the transmission of the contraction between the dilated baseplate and the sheath. As seen in phage T4[5], AFP particle[19], and pyocin R2[11], the rearrangements in the sheath adaptor trigger further conformational changes along the sheath, without affecting its structural integrity. The compaction and diameter expansion of the contracted sheath lead to tube-sheath detachment and tube ejection, with final perforation of the target cell membrane to inject the payload into the target cell (Fig. 7). The puncturing end of the tube, which is sharpened by the central spike and spike tip, is crucial for the perforation. Both the rigidity of the spike and the conical shape of the tip play important roles in the piercing process. Indeed, the rigid spike is believed to translocate through the membrane without major unfolding and, in some phages, loaded with ions[37,38]. Our analysis of the sequence and predicted structure of the spike tip protein Pvc10 suggests the hypothesis of potential loading of sodium ions in the tip, which may contribute to target cell membrane digestion during piercing.

Upon perforation, PVCs can translocate toxins through eukaryotic cell membranes[21,22]. Functional studies employing PVCs have demonstrated specific delivery of protein cargoes into selected target cells, together with efficient reprograming of receptor recognition by tail fibers[28,29]. The ability of modified PVCs to recognize and deliver payloads to specific targets could be harnessed for the development of targeted drug delivery systems. The identification of key structural features involved in contraction and target selection is crucial for broadening the opportunities to engineer PVCs with modified host recognition properties and customized cargo-loading capabilities.

In conclusion, by elucidating structural features of the *Pl*PVC1 particle, together with transitions between extended and contracted states, this study enhances our understanding of contractile injection systems and their evolutionary links to bacteriophages. The findings presented here deepen our knowledge of bacterial nanomachines and lay more groundwork for harnessing PVCs in biomedical and agricultural applications. Future research should aim to characterize the full spectrum of effector payloads delivered by these systems, investigate their functional mechanisms, and explore engineering strategies to optimize PVCs for use as versatile biotechnological tools.

Methods

Experimental model and subject details

E. coli strains were cultured aerobically in Luria-Bertani (LB) medium [1% (w/v) NaCl; 1% (w/v) tryptone; 0.5% (w/v) yeast extract] at 37 °C. *E. coli* HST08 strain (Stellar chemically competent cells) was used for DNA manipulation, and *E. coli* BL21Star(DE3) was used for protein expression.

Photorhabdus luminescens DJC strain (TT01-RifR) was obtained from the lab of Prof. Dr. Ralf Heermann (Johannes Gutenberg University of Mainz, Germany). This strain was cultivated aerobically in CASO medium [5% (w/v) NaCl; 1.5% (w/v) peptone from casein; 0.5% (w/v) peptone from soymeal] at 30 °C.

For the preparation of agar plates, 1% (w/v) agar was added to the respective medium. Antibiotics were used as follows: ampicillin 100 µg/mL; chloramphenicol 34 µg/mL; rifampicin 50 µg/mL.

Cloning of the *Pl*PVC1 encoding operon

The *pvc* operon 1 from *Photorhabdus luminescens DJC, Plpvc1* (*PluDJC_08925* to *PluDJC_08830*) was amplified by PCR from genomic DNA and cloned into pBAD33 plasmid (arabinose-inducible promoter, chloramphenicol resistance), previously linearized by PCR, using primers with an overlap with the first and last ORF in the *Plpvc1* cluster (Supplementary Table 6). After DNA fragment purification, insert and vector were mixed in a 1:1 ratio and incubated with In-Fusion® Snap Assembly Master Mix (Takara) for 15 min at 50 °C. *E. coli* Stellar competent cells were transformed with 2.5 µL of In-Fusion reaction and incubated overnight. Positive clones were screened by colony PCR and restriction enzyme digestion (BamHI and BsaI) after plasmid extraction. The full plasmid sequence was verified by Next Generation Sequencing. PCR reactions were performed with Platinum™ SuperFi™ PCR Master Mix (Invitrogen), and DNA fragment purification was carried out using QIAGEX II Gel Extraction kit (Qiagen).

*Pl*PVC1 particle expression

Verified pBAD33-PluDJC_08925-08830 plasmid was transformed into *E. coli* BL21Star(DE3) electrocompetent cells. After selection, cells were grown overnight at 37 °C in 10 mL LB medium supplemented with chloramphenicol. The following day, 1 L of LB medium supplemented with chloramphenicol was inoculated with an overnight culture, and protein expression was induced with 0.2% L-Arabinose at an OD_{600} of 0.7. Cells were incubated for 24 h at 18 °C with slow agitation (80 rpm). Then, cells were harvested at 4000 × *g* for 20 min at 4 °C. The cell pellet was resuspended in 50 mL of cold Milli-Q water. Washing was carried out by centrifugation at 4000 × *g* for 15 min at 4 °C. The final pellet was flash-frozen in liquid nitrogen for 5 min and stored at −20 °C.

*Pl*PVC1 particle purification

Bacterial cell pellets were lysed in 25 mL of lysis buffer[27] (25 mM Tris pH 7.4, 140 mM NaCl, 3 mM KCl, 200 µg/mL lysozyme, 50 µg/mL DNase I, 0.5% Triton X-100, 5 mM $MgCl_2$, 1× protease inhibitor) for 1 h at 37 °C. The cell lysate was cleared by two rounds of centrifugation (6000 × *g* for 30 min at 4 °C, and 30,000 × *g* for 30 min at 4 °C). The particles were pelleted by ultracentrifugation at 100,000 × *g* for 1 h at 4 °C. The particle pellet was resuspended overnight in 2 mL of Tris-salt buffer[20] (20 mM Tris, pH 7.5, 150 mM NaCl). The resuspension was applied on an iodixanol-based gradient (10%-40%) and subjected to ultracentrifugation at 100,000 × *g* for 20 h at 4 °C. The gradient was divided into 12 fractions, and each fraction was checked for the presence of *Pl*PVC1 particles by NS-TEM. The fractions containing the particles were buffer-exchanged (from iodixanol to Tris-salt buffer) via dialysis in 20 kDa MWCO cassettes for 6 days at 4 °C. After dialysis, particles were pelleted by ultracentrifugation at 100,000 × *g* for 1 h at 4 °C. The pellet was finally resuspended in 100 µL of Tris-salt buffer and cleared by centrifugation at 10,000 × *g* for 5 min at 4 °C. The supernatant containing the *Pl*PVC1 particles was stored at 4 °C for short-term use.

Mass spectrometry sample preparation

100 µL of room-temperature (25 °C) 50 mM ammonium bicarbonate was added to 20 µg (in ~5 µL) of purified *Pl*PVC1 sample. Following this, 0.5 µg of sequencing-grade trypsin was added, and the sample was incubated overnight at 25 °C with gentle mixing. The digest was reduced and alkylated by concomitant addition of tris(2-carboxyethyl) phosphine and chloroacetamide to final concentrations of 10 mM, and incubating at 30 °C for 30 min. The sample was clarified through a 0.45 µm spin filter, and peptides were purified via a high-pH C18 StageTip procedure. To this end, C18 StageTips were prepared in-house by layering four plugs of C18 material (Sigma-Aldrich, Empore SPE Disks, C18, 47 mm) per StageTip. Activation of StageTips was performed with 100 µL 100% methanol, followed by equilibration using 100 µL 80% acetonitrile (ACN) in 200 mM ammonium hydroxide, and two washes with 100 µL 50 mM ammonium hydroxide. The sample was basified to pH >10 by the addition of one tenth volume of 200 mM ammonium hydroxide, and loaded on two StageTips. Subsequently, StageTips were washed twice using 100 µL 50 mM ammonium hydroxide, after which peptides were eluted using 80 µL 25% ACN in 50 mM ammonium hydroxide. The samples were dried to completion using a SpeedVac at 60 °C. Dried peptides were dissolved in 20 µL 0.1% formic acid (FA) and stored at −20 °C until analysis using mass spectrometry.

Mass spectrometry data acquisition

Around 2 µg of digested proteins (~500 ng of peptide) were analyzed per injection, with three technical replicates ($n = 3$). All analyses were performed on an EASY-nLC 1200 system (Thermo) coupled to an Orbitrap Exploris 480 mass spectrometer (Thermo). Samples were analyzed on 20 cm long analytical columns, with an internal diameter of 75 µm, and packed in-house using ReproSil-Pur 120 C18-AQ 1.9 µm beads (Dr. Maisch). The analytical column was heated to 40 °C, and elution of peptides from the column was achieved by application of gradients with stationary phase Buffer A (0.1% FA) and increasing amounts of mobile phase Buffer B (80% ACN in 0.1% FA). The primary analytical gradients ranged from 5 % Buffer B to 38 % Buffer B over 60 min, followed by a further increase to 48 % Buffer B over 5 min to elute any remaining peptides, and finally a washing block of 15 min. Ionization was achieved using a NanoSpray Flex NG ion source (Thermo), with spray voltage set at 2 kV, ion transfer tube temperature to 275 °C, and RF funnel level to 40%. Full scan range was set to 300–1,300 m/z, MS1 resolution to 120,000, MS1 AGC target to "200" (2,000,000 charges), and MS1 maximum injection time to "Auto". Precursors with charges 2–6 were selected for fragmentation using an isolation width of 1.3 m/z and fragmented using higher-energy collision dissociation (HCD) with a normalized collision energy of 25. Monoisotopic Precursor Selection (MIPS) was enabled in "Peptide" mode. Precursors were prevented from being repeatedly sequenced by setting dynamic exclusion duration to 80 s, with an exclusion mass tolerance of 15 ppm and exclusion of isotopes. MS/MS resolution was set to 30,000, MS/MS AGC target to "200" (200,000 charges), MS/MS intensity threshold to 360,000 charges/second, MS/MS maximum injection time to "Auto", and number of dependent scans (TopN) to 13.

Mass spectrometry data analysis

All RAW files were analyzed using MaxQuant software[47,48] v1.5.3.30. Default MaxQuant settings were used, with exceptions outlined below. For the generation of the theoretical spectral library, all expected full-length PVC protein sequences were entered into a FASTA database. Digestion was performed using "Trypsin/P" (default), allowing up to 3 missed cleavages. Minimum peptide length was set to 6, and maximum peptide mass to 6000 Da. Carbamidomethylation of cysteine residues was set as a fixed modification (default). Protein N-terminal acetylation (default), oxidation of methionine (default), deamidation of asparagine and glutamine, and peptide N-terminal glutamine to pyroglutamate were included as potential variable modifications, with a maximum allowance of 3 variable modifications per peptide. Modified peptides were stringently filtered by setting a minimum score of 100 and a minimum delta score of 50. First, the search mass tolerance was set to 10 ppm, and the maximum charge state of the considered precursors was set to 6. Final search mass tolerance was 4.5 ppm (default), with a fragment mass tolerance of 20 ppm (default). Label-free quantification (LFQ) was enabled, with "Fast LFQ" disabled. The second peptide search was disabled. Matching between runs was enabled with a match time window of 1 min and an alignment time window of 20 min. Data was filtered by posterior error probability to achieve a false discovery rate of <1% (default), at the peptide-spectrum match, protein assignment, and site-decoy levels.

*Pl*PVC1 particle contraction

Particle contraction was performed via dialysis in 3 M urea[31,32]. 70 µL of purified *Pl*PVC1 sample were placed in a mini dialysis cassette of 20 kDa MWCO. The sample was first dialyzed for 4 h in 3 M urea, pH 7.5, at 4 °C, and then dialyzed in Tris-salt buffer for another 4 h at 4 °C. The contracted sample was stored at 4 °C until further use.

Negative-staining transmission electron microscopy

For NS-TEM, 4 µL of *Pl*PVC1 samples were applied onto glow-discharged (30 s, 15 mA, in a Leica ACE 200) copper grids (200 mesh, coated with a continuous carbon layer), then washed 3 times with 50 µL milli-Q water, and finally stained with 2% uranyl acetate. The grids were dried at room temperature and imaged on a Morgagni 268 transmission electron microscope operated at 100 kV (FEI/Philips), equipped with a side-mounted Olympus Veleta camera with a resolution of 2048 × 2048 pixels (2 K × 2 K). Images were recorded using ITEM software.

Cryo-EM grid preparation

For cryo-EM, 3 µL of *Pl*PVC1 samples were applied to glow-discharged (10 s, 5 mA, in a Leica ACE 200) Quantifoil grids (R2/2, 200 mesh Gold, coated with a 2 nm continuous carbon layer), and plunge-frozen into liquid ethane pre-cooled with liquid nitrogen, using a Vitrobot Mark IV (FEI, Thermo Fisher Scientific) at 4 °C and 100% humidity.

Cryo-EM data collection, image processing, and refinement

The cryo-EM grids were screened on a Glacios cryo-TEM at 200 kV (Thermo Fisher Scientific), equipped with a Falcon 3 Direct Electron Detector. Data acquisition was performed on a Titan Krios G2 at 300 kV (Thermo Fisher Scientific), equipped with a Falcon 4i Direct Electron Detector and SelectrisX energy filter. Micrographs were collected using the semi-automated acquisition program EPU (FEI, Thermo Fisher Scientific) at 105,000× magnification, with a calibrated pixel size of 1.2 Å and a defocus range of −0.6 to −2.0 µm.

All datasets were processed using cryoSPARC[49] v4.3.0 to v4.6.2. First, patch motion correction was used to estimate and correct for full-frame motion and sample deformation (local motion). Patch contrast transfer function (CTF) estimation was used to fit a local CTF to micrographs. Micrographs were manually curated to remove low-quality data based on ice thickness, local-motion distances, and CTF-fit parameters. Particles were picked using Topaz particle picking[50]. First, Topaz was trained with a manually picked set of particles. Then, Topaz Extract was used with the pre-trained model and a pre-tested particle threshold value. This procedure was performed equally for the baseplate of the extended particle, the cap, and the baseplate of the contracted particle.

Baseplate. After Topaz particle picking and picks inspection, particles were extracted with a box size of 700 pixels and Fourier-cropped to 352 pixels. One round of 2D classification was performed, followed by ab initio 3D reconstruction. The 3D density was refined by non-uniform refinement, with imposed C6 symmetry. After particle re-extraction with full box size (700 pixels), non-uniform refinement, with imposed C6 symmetry, was applied with a dynamic mask to obtain a high-resolution map.

Central spike. The C6-symmetrized 3D volume of the baseplate was shifted toward the central spike region, and particles were re-extracted with a box size of 360 pixels. After 3D reconstruction and refinement, particles were subjected to symmetry expansion (total copies = 6). One round of 3D classification, with a focus mask around the central spike region, was performed. The density of the one class showing clear trimeric symmetry was refined by non-uniform refinement with C3 symmetry imposed. Duplicated particles were removed, and the final high-resolution map of the central spike region was obtained by non-uniform refinement with imposed C3 symmetry.

Fiber. Particles from the binned C6-symmetrized 3D volume of the baseplate were re-extracted with a box size of 560 pixels and a binning factor of 1.25×. After 3D reconstruction and refinement, particles were subjected to symmetry expansion (total copies = 6). Two rounds of 3D classification, with a focus mask around the fiber, were performed. Classes showing clear density in the masked area were refined by local refinement without symmetry imposition (C1), using the same mask applied during the 3D classifications.

Cap. After Topaz particle picking and pick inspection, particles were extracted with a box size of 560 pixels and Fourier-cropped to 288 pixels. One round of 2D classification was performed, followed by ab initio 3D reconstruction. The 3D density was refined by non-uniform refinement, with imposed C6 symmetry. After particle re-extraction with full box size (560 pixels), non-uniform refinement with imposed C6 symmetry was applied with a dynamic mask to obtain a high-resolution map.

Baseplate of the contracted particle. After Topaz particle picking and pick inspection, particles were extracted with a box size of 700 pixels and Fourier-cropped to 352 pixels. One round of 2D classification was performed, followed by ab initio 3D reconstruction. The 3D density was refined by heterogeneous and non-uniform refinement, with imposed C6 symmetry. Particles were subjected to symmetry expansion (total copies = 6). One round of 3D classification, with a focus mask around one baseplate wedge, was performed. The class showing clear density in the masked area was refined by local refinement without symmetry imposition (C1), using the same mask used for the 3D classification. Duplicated particles were removed, and the 3D density was refined by homogeneous refinement with imposed C6 symmetry. After particle re-extraction with full box size (700 pixels), homogeneous refinement with imposed C6 symmetry was applied to obtain a higher-resolution map.

Contracted sheath. The binned C6-symmetrized 3D volume of the baseplate of the contracted particle was subjected to local refinement, with imposed C6 symmetry and focus mask surrounding the first layers of the sheath immediately after the baseplate. One round of 3D classification, using the same focus mask, was performed. The class showing clear density in the masked area was refined by local refinement with imposed C6 symmetry. After particle re-extraction with full box size (700 pixels), local refinement with imposed C6 symmetry was applied to obtain a high-resolution map.

All the applied masks were created in UCSF ChimeraX[51] v1.8 and processed in cryoSPARC[49]. For all datasets, the number of micrographs, total exposure values, particles used for final refinement, map resolution, and other values during data processing are summarized in Supplementary Table 3. Cryo-EM data processing workflow and map resolutions with GSFSC curves are summarized in Supplementary Figs. 3 and 4.

Model building

The initial models of each protein in the *Pl*PVC1 particle were predicted with AlphaFold2[52] using the full-length amino acid sequences. Starmap[53] v1.1.75 was used for automated building of the best-ranked AlphaFold2-predicted models in the density maps. Starmap results were inspected and manually adjusted in ISOLDE[54] and Coot[55]. Atomic models were then refined against the corresponding maps using phenix.real_space_refine[56] with secondary structure restraints and geometry restraints. Several iterations of phenix.real_space_refine, followed by manual adjustments in ISOLDE and Coot, were performed until convergence. Atomic models of Pvc6 and the interaction between Pvc12 and Pvc13 were partially built due to density limitations. The atomic model of the baseplate of the contracted particle was generated by rigid-body fitting of the baseplate wedge proteins and the sheath adaptor into the solved density. A summary of the model refinement and validation statistics can be found in Supplementary Table 3, and the full-length amino acid sequences for each protein in the *Pl*PVC1 particle are provided in Supplementary Data 1.

Bioinformatics analysis

Multiple sequence alignments (MSA) were performed using Clustal Omega[57] and visualized using ESPript 3.0[58]. DALI web server[35] and Foldseek Search Server[36] were used for structural analysis and comparison. Protein interaction interfaces were predicted using the parameter-free geometric deep learning method PeSTo[33,34] (Protein Structure Transformer). ConSurf Server[59] was used for conservation analysis of sequence profiles. The full-length amino acid sequences used for these analyses are provided in Supplementary Data 1–2. The MSAs generated by the ConSurf server are provided as Supplementary Data 3–15.

Reporting summary

Further information on research design is available in the Nature Portfolio Reporting Summary linked to this article.

Data availability

The cryo-EM density maps and the corresponding atomic coordinates have been deposited in the Electron Microscopy Data Bank (EMDB) and in the Protein Data Bank (PDB), respectively. The accession codes are listed as follows: baseplate (EMD-53137, 9QGL); central spike (EMD-53138, 9QGM); cap (EMD-53139, 9QGN); fiber and baseplate-fiber interaction (EMD-53140, 9QGO); contracted sheath (EMD-53141, 9QGP); baseplate of the contracted particle (EMD-53143). The raw cryo-EM datasets used in this study have been deposited in the Electron Microscopy Public Image Archive (EMPIAR)[60]: dataset *Pl*PVC1 particle in extended state under the accession code EMPIAR-12841, and dataset *Pl*PVC1 particle in contracted state under the accession code EMPIAR-12848. The mass spectrometry proteomics data have been deposited to the ProteomeXchange Consortium via the PRIDE[61] partner repository with the dataset identifier PXD060336. Source data are provided as a Source Data file. Source data are provided with this paper.

References

1. Hibbing, M. E., Fuqua, C., Parsek, M. R. & Peterson, S. B. Bacterial competition: surviving and thriving in the microbial jungle. *Nat. Rev. Microbiol.* **8**, 15–25 (2010).
2. Galán, J. E. & Waksman, G. Protein-injection machines in bacteria. *Cell* **172**, 1306–1318 (2018).
3. Kooger, R., Szwedziak, P., Böck, D. & Pilhofer, M. CryoEM of bacterial secretion systems. *Curr. Opin. Struct. Biol.* **52**, 64–70 (2018).
4. Taylor, N. M. I., Van Raaij, M. J. & Leiman, P. G. Contractile injection systems of bacteriophages and related systems. *Mol. Microbiol.* **108**, 6–15 (2018).
5. Taylor, N. M. I. et al. Structure of the T4 baseplate and its function in triggering sheath contraction. *Nature* **533**, 346–352 (2016).
6. Leiman, P. G. et al. Type VI secretion apparatus and phage tail-associated protein complexes share a common evolutionary origin. *Proc. Natl. Acad. Sci. USA* **106**, 4154–4159 (2009).
7. Brackmann, M., Wang, J. & Basler, M. Type VI secretion system sheath inter-subunit interactions modulate its contraction. *EMBO Rep.* **19**, 225–233 (2018).
8. Wang, J., Brodmann, M. & Basler, M. Assembly and subcellular localization of bacterial type VI secretion systems. *Annu. Rev. Microbiol.* **73**, 621–638 (2019).
9. Ghequire, M. G. K. & De Mot, R. The tailocin tale: peeling off phage tails. *Trends Microbiol.* **23**, 587–590 (2015).
10. Michel-Briand, Y. & Baysse, C. The pyocins of Pseudomonas aeruginosa. *Biochimie* **84**, 499–510 (2002).
11. Ge, P. et al. Action of a minimal contractile bactericidal nanomachine. *Nature* **580**, 658–662 (2020).
12. Köhler, T., Donner, V. & Van Delden, C. Lipopolysaccharide as shield and receptor for R-pyocin-mediated killing in *Pseudomonas aeruginosa*. *J. Bacteriol.* **192**, 1921–1928 (2010).
13. Uratani, Y. & Hoshino, T. Pyocin R1 inhibits active transport in Pseudomonas aeruginosa and depolarizes membrane potential. *J. Bacteriol.* **157**, 632–636 (1984).
14. Shikuma, N. J. et al. Marine tubeworm metamorphosis induced by arrays of bacterial phage tail–like structures. *Science* **343**, 529–533 (2014).
15. Ericson, C. F. et al. A contractile injection system stimulates tubeworm metamorphosis by translocating a proteinaceous effector. *eLife* **8**, e46845 (2019).
16. Rocchi, I. et al. A Bacterial phage tail-like structure kills eukaryotic cells by injecting a nuclease effector. *Cell Rep.* **28**, 295–301.e4 (2019).
17. Hurst, M. R. H., Glare, T. R. & Jackson, T. A. Cloning Serratia entomophila antifeeding genes-a putative defective prophage active against the grass grub Costelytra zealandica. *J. Bacteriol.* **186**, 5116–5128 (2004).
18. Hurst, M. R. H., Beard, S. S., Jackson, T. A. & Jones, S. M. Isolation and characterization of the Serratia entomophila antifeeding prophage. *FEMS Microbiol. Lett.* **270**, 42–48 (2007).
19. Desfosses, A. et al. Atomic structures of an entire contractile injection system in both the extended and contracted states. *Nat. Microbiol.* **4**, 1885–1894 (2019).
20. Xu, J. et al. Identification and structure of an extracellular contractile injection system from the marine bacterium Algoriphagus machipongonensis. *Nat. Microbiol.* **7**, 397–410 (2022).
21. Yang, G., Dowling, A. J., Gerike, U., ffrench-Constant, R. H. & Waterfield, N. R. Photorhabdus virulence cassettes confer injectable insecticidal activity against the wax moth. *J. Bacteriol.* **188**, 2254–2261 (2006).
22. Vlisidou, I. et al. The Photorhabdus asymbiotica virulence cassettes deliver protein effectors directly into target eukaryotic cells. *eLife* **8**, e46259 (2019).
23. Hapeshi, A. & Waterfield, N. R. Photorhabdus asymbiotica as an Insect and Human Pathogen. In *The Molecular Biology of Photorhabdus Bacteria* (ed. ffrench-Constant, R. H.) vol. 402 159–177 (Springer International Publishing, Cham, 2016).
24. Wilkinson, P. et al. Comparative genomics of the emerging human pathogen Photorhabdus asymbiotica with the insect pathogen Photorhabdus luminescens. *BMC Genomics* **10**, 302 (2009).
25. Sarris, P. F., Ladoukakis, E. D., Panopoulos, N. J. & Scoulica, E. V. A phage tail-derived element with wide distribution among both prokaryotic domains: a comparative genomic and phylogenetic study. *Genome Biol. Evol.* **6**, 1739–1747 (2014).
26. Chen, L. et al. Genome-wide identification and characterization of a superfamily of bacterial extracellular contractile injection systems. *Cell Rep.* **29**, 511–521.e2 (2019).
27. Jiang, F. et al. Cryo-EM structure and assembly of an extracellular contractile injection system. *Cell* **177**, 370–383.e15 (2019).
28. Kreitz, J. et al. Programmable protein delivery with a bacterial contractile injection system. *Nature* **616**, 357–364 (2023).
29. Jiang, F. et al. N-terminal signal peptides facilitate the engineering of PVC complex as a potent protein delivery system. *Sci. Adv.* **8**, eabm2343 (2022).
30. Zamora-Lagos, M.-A. et al. Phenotypic and genomic comparison of Photorhabdus luminescens subsp. laumondii TT01 and a widely used rifampicin-resistant Photorhabdus luminescens laboratory strain. *BMC Genomics* **19**, 854 (2018).
31. Leiman, P. G., Chipman, P. R., Kostyuchenko, V. A., Mesyanzhinov, V. V. & Rossmann, M. G. Three-dimensional rearrangement of proteins in the tail of bacteriophage T4 on infection of its host. *Cell* **118**, 419–429 (2004).
32. Hu, B., Margolin, W., Molineux, I. J. & Liu, J. Structural remodeling of bacteriophage T4 and host membranes during infection initiation. *Proc. Natl. Acad. Sci. USA* **112**, E4919–E4928 (2015).
33. Krapp, L. F., Abriata, L. A., Cortés Rodriguez, F. & Dal Peraro, M. PeSTo: parameter-free geometric deep learning for accurate prediction of protein binding interfaces. *Nat. Commun.* **14**, 2175 (2023).

34. Bibekar, P., Krapp, L. & Peraro, M. D. PeSTo-Carbs: geometric deep learning for prediction of protein–carbohydrate binding interfaces. *J. Chem. Theory Comput.* **20**, 2985–2991 (2024).
35. Holm, L., Laiho, A., Törönen, P. & Salgado, M. DALI shines a light on remote homologs: One hundred discoveries. *Protein Sci.* **32**, e4519 (2023).
36. Van Kempen, M. et al. Fast and accurate protein structure search with Foldseek. *Nat. Biotechnol.* **42**, 243–246 (2024).
37. Kanamaru, S. et al. Structure of the cell-puncturing device of bacteriophage T4. *Nature* **415**, 553–557 (2002).
38. Browning, C., Shneider, M. M., Bowman, V. D., Schwarzer, D. & Leiman, P. G. Phage pierces the host cell membrane with the iron-loaded spike. *Structure* **20**, 326–339 (2012).
39. Bateman, A. & Bycroft, M. The structure of a LysM domain from E. coli membrane-bound lytic murein transglycosylase D (MltD). *J. Mol. Biol.* **299**, 1113–1119 (2000).
40. Ge, P. et al. Atomic structures of a bactericidal contractile nanotube in its pre- and postcontraction states. *Nat. Struct. Mol. Biol.* **22**, 377–382 (2015).
41. Fokine, A. et al. The molecular architecture of the bacteriophage T4 neck. *J. Mol. Biol.* **425**, 1731–1744 (2013).
42. Weiss, G. L. et al. Structure of a thylakoid-anchored contractile injection system in multicellular cyanobacteria. *Nat. Microbiol.* **7**, 386–396 (2022).
43. Crawford, J. T. & Goldberg, E. B. The function of tail fibers in triggering baseplate expansion of bacteriophage T4. *J. Mol. Biol.* **139**, 679–690 (1980).
44. Bertozzi Silva, J., Storms, Z. & Sauvageau, D. Host receptors for bacteriophage adsorption. *FEMS Microbiol. Lett.* **363**, fnw002 (2016).
45. Maghsoodi, A., Chatterjee, A., Andricioaei, I. & Perkins, N. C. How the phage T4 injection machinery works including energetics, forces, and dynamic pathway. *Proc. Natl. Acad. Sci. USA* **116**, 25097–25105 (2019).
46. Dams, D., Brøndsted, L., Drulis-Kawa, Z. & Briers, Y. Engineering of receptor-binding proteins in bacteriophages and phage tail-like bacteriocins. *Biochem. Soc. Trans.* **47**, 449–460 (2019).
47. Cox, J. & Mann, M. MaxQuant enables high peptide identification rates, individualized p.p.b.-range mass accuracies and proteome-wide protein quantification. *Nat. Biotechnol.* **26**, 1367–1372 (2008).
48. Cox, J. et al. Andromeda: a peptide search engine integrated into the MaxQuant environment. *J. Proteome Res.* **10**, 1794–1805 (2011).
49. Punjani, A., Rubinstein, J. L., Fleet, D. J. & Brubaker, M. A. cryoSPARC: algorithms for rapid unsupervised cryo-EM structure determination. *Nat. Methods* **14**, 290–296 (2017).
50. Bepler, T. et al. Positive-unlabeled convolutional neural networks for particle picking in cryo-electron micrographs. *Nat. Methods* **16**, 1153–1160 (2019).
51. Pettersen, E. F. et al. UCSF ChimeraX: structure visualization for researchers, educators, and developers. *Protein Sci.* **30**, 70–82 (2021).
52. Jumper, J. et al. Highly accurate protein structure prediction with AlphaFold. *Nature* **596**, 583–589 (2021).
53. Lugmayr, W. et al. StarMap: a user-friendly workflow for Rosetta-driven molecular structure refinement. *Nat. Protoc.* **18**, 239–264 (2023).
54. Croll, T. I. *ISOLDE*: a physically realistic environment for model building into low-resolution electron-density maps. *Acta Crystallogr. Sect. Struct. Biol.* **74**, 519–530 (2018).
55. Emsley, P., Lohkamp, B., Scott, W. G. & Cowtan, K. Features and development of *Coot*. *Acta Crystallogr. D. Biol. Crystallogr.* **66**, 486–501 (2010).
56. Liebschner, D. et al. Macromolecular structure determination using X-rays, neutrons and electrons: recent developments in *Phenix*. *Acta Crystallogr. Sect. Struct. Biol.* **75**, 861–877 (2019).
57. Sievers, F. & Higgins, D. G. Clustal omega. *Curr. Protoc. Bioinform.* **48**, 3.13.1–3.13.16 (2014).
58. Robert, X. & Gouet, P. Deciphering key features in protein structures with the new ENDscript server. *Nucleic Acids Res.* **42**, W320–W324 (2014).
59. Ashkenazy, H. et al. ConSurf 2016: an improved methodology to estimate and visualize evolutionary conservation in macromolecules. *Nucleic Acids Res.* **44**, W344–W350 (2016).
60. Iudin, A. et al. EMPIAR: the Electron Microscopy Public Image Archive. *Nucleic Acids Res.* **51**, D1503–D1511 (2023).
61. Perez-Riverol, Y. et al. The PRIDE database at 20 years: 2025 update. *Nucleic Acids Res.* **53**, D543–D553 (2025).

Acknowledgements

The Novo Nordisk Foundation Center for Protein Research is supported financially by the Novo Nordisk Foundation (NNF14CC0001). This work was supported by an NNF Hallas-Møller Emerging Investigator grant (NNF17OC0031006), an NNF Hallas-Møller Ascending Investigator grant (NNF23OC0081528), and an LF Ascending Investigator grant (R434-2023-289) to N.M.I.T., who is a member of the Integrative Structural Biology Cluster (ISBUC) at the University of Copenhagen. This work was also supported by a fellowship from laCaixa Foundation (ID 100010434) with code LCF/BQ/EU21/11890147 to L.M.A. We acknowledge the Danish Cryo-EM Facility at the Core Facility for Integrated Microscopy (CFIM) at the University of Copenhagen for support during data collection. We acknowledge the Big Data Management Platform at the Novo Nordisk Foundation Center for Protein Research for the computational resources.

Author contributions

L.M.A., N.M.I.T., and E.M.S.R. conceived the project. L.M.A. performed cloning, particle expression, and particle purification and contraction. I.A.H. performed mass spectrometry and analyzed the data, in consultation with M.L.N. L.M.A. and A.R.E. prepared cryo-EM grids and collected cryo-EM data, with assistance of T.P. and N.S. L.M.A. and A.R.E. processed the cryo-EM data and determined the structures presented in this study. L.M.A. performed the bioinformatic analysis. N.M.I.T. and L.M.A. acquired the financial support for the project. L.M.A. wrote the manuscript and prepared the figures, with input from all authors. All authors contributed to the revision of the manuscript.

Competing interests

Eva Maria Steiner-Rebrova and Nicholas M. I. Taylor are inventors on a patent application related to eCIS (PCT/EP2023/068102). Eva Maria Steiner-Rebrova is co-founder of Yngvi Bio ApS. The other authors declare no competing interests.

Additional information

Supplementary information The online version contains supplementary material available at https://doi.org/10.1038/s41467-025-64377-z.

Correspondence and requests for materials should be addressed to Nicholas M. I. Taylor.

Peer review information *Nature Communications* thanks the anonymous reviewers for their contribution to the peer review of this work. A peer review file is available.